

Radiative Cooling, Latent Heating, and Cloud Ice in the Tropical Upper Troposphere

Adam Sokol¹ and Dennis Hartmann¹

¹University of Washington Seattle

November 22, 2022

Abstract

The radiative cooling rate in the tropical upper troposphere is expected to increase as climate warms. Since the tropics are approximately in radiative-convective equilibrium (RCE), this implies an increase in the convective heating rate, which is the sum of the latent heating rate and the eddy heat flux convergence. We examine the impact of these changes on the vertical profile of cloud ice amount in cloud-resolving simulations of RCE. Three simulations are conducted: a control run, a warming run, and an experimental run in which there is no warming but a temperature forcing is imposed to mimic the warming-induced increase in radiative cooling. Surface warming causes a reduction in cloud fraction at all upper tropospheric temperature levels but an increase in the ice mixing ratio within deep convective cores. The experimental run has more cloud ice than the warming run at fixed temperature despite the fact that their latent heating rates are equal, which suggests that the efficiency of latent heating by cloud ice increases with warming. An analytic expression relating the ice-related latent heating rate to a number of other factors is derived and used to understand the model results. This reveals that the increase in latent heating efficiency is driven mostly by 1) the migration of isotherms to lower pressure and 2) a slight warming of the top of the convective layer. These physically robust changes act to reduce the residence time of ice along at any particular temperature level, which tempers the response of the mean cloud ice profile to warming.

Journal of Climate

Radiative Cooling, Latent Heating, and Cloud Ice in the Tropical Upper Troposphere

--Manuscript Draft--

Manuscript Number:	JCLI-D-21-0444
Full Title:	Radiative Cooling, Latent Heating, and Cloud Ice in the Tropical Upper Troposphere
Article Type:	Article
Corresponding Author:	Adam Bennett Sokol University of Washington Seattle, WA UNITED STATES
Corresponding Author's Institution:	University of Washington
First Author:	Adam B Sokol
Order of Authors:	Adam B Sokol Dennis L Hartmann
Abstract:	<p>The radiative cooling rate in the tropical upper troposphere is expected to increase as climate warms. Since the tropics are approximately in radiative-convective equilibrium (RCE), this implies an increase in the convective heating rate, which is the sum of the latent heating rate and the eddy heat flux convergence. We examine the impact of these changes on the vertical profile of cloud ice amount in cloud-resolving simulations of RCE. Three simulations are conducted: a control run, a warming run, and an experimental run in which there is no warming but a temperature forcing is imposed to mimic the warming-induced increase in radiative cooling. Surface warming causes a reduction in cloud fraction at all upper tropospheric temperature levels but an increase in the ice mixing ratio within deep convective cores. The experimental run has more cloud ice than the warming run at fixed temperature despite the fact that their latent heating rates are equal, which suggests that the efficiency of latent heating by cloud ice increases with warming. An analytic expression relating the ice-related latent heating rate to a number of other factors is derived and used to understand the model results. This reveals that the increase in latent heating efficiency is driven mostly by 1) the migration of isotherms to lower pressure and 2) a slight warming of the top of the convective layer. These physically robust changes act to reduce the residence time of ice along at any particular temperature level, which tempers the response of the mean cloud ice profile to warming.</p>

1 **Radiative Cooling, Latent Heating, and Cloud Ice in the Tropical Upper**

2 **Troposphere**

3 Adam B. Sokol* and Dennis L. Hartmann[†]

4 *Department of Atmospheric Sciences, University of Washington, Seattle, WA 98195*

5 *Corresponding author: Adam B. Sokol, abs66@uw.edu

6 [†]Current affiliation: Department of Atmospheric Sciences, University of Washington, Seattle, WA

ABSTRACT

7 The radiative cooling rate in the tropical upper troposphere is expected to increase as climate
8 warms. Since the tropics are approximately in radiative-convective equilibrium (RCE), this implies
9 an increase in the convective heating rate, which is the sum of the latent heating rate and the eddy
10 heat flux convergence. We examine the impact of these changes on the vertical profile of cloud ice
11 amount in cloud-resolving simulations of RCE. Three simulations are conducted: a control run,
12 a warming run, and an experimental run in which there is no warming but a temperature forcing
13 is imposed to mimic the warming-induced increase in radiative cooling. Surface warming causes
14 a reduction in cloud fraction at all upper tropospheric temperature levels but an increase in the
15 ice mixing ratio within deep convective cores. The experimental run has more cloud ice than the
16 warming run at fixed temperature despite the fact that their latent heating rates are equal, which
17 suggests that the efficiency of latent heating by cloud ice increases with warming. An analytic
18 expression relating the ice-related latent heating rate to a number of other factors is derived and
19 used to understand the model results. This reveals that the increase in latent heating efficiency is
20 driven mostly by 1) the migration of isotherms to lower pressure and 2) a slight warming of the
21 top of the convective layer. These physically robust changes act to reduce the residence time of ice
22 along at any particular temperature level, which tempers the response of the mean cloud ice profile
23 to warming.

24 *Significance statement.* Here we examine how the amount of condensed ice in part of the atmo-
25 sphere—the tropical upper troposphere (UT)—responds to global warming. In the UT, the energy
26 released during ice formation is balanced by the emission of radiation to space. This emission will
27 strengthen with warming, suggesting that there will also be more ice. Using a model of the tropical
28 atmosphere, we find that the increase in ice amount is mitigated by a reduction in the amount of
29 time ice spends in the UT. This could have important implications for the cloud response to global
30 warming, and future work should focus on how these changes are manifested across the distribution
31 of convective cloud types.

32 **1. Introduction**

33 Ice clouds produced by tropical convection play an important role in Earth’s climate yet remain
34 a significant source of uncertainty in projections of climate change (Bony et al. 2015; Zelinka et al.
35 2017). Changes in the properties and abundance of deep convective cores and their associated anvil
36 clouds could have wide implications for the tropical radiation budget and global climate (Zelinka
37 et al. 2012; Hartmann 2016). Predicting these changes requires an understanding of complex
38 dynamic, microphysical, and radiative processes that are difficult to observe and model. This
39 complexity is evident in the Radiative-Convective Equilibrium Model Intercomparison Project
40 (RCEMIP), in which different cloud-resolving models (CRMs) with nearly identical domains
41 produce wildly different cloud climatologies and cloud responses to warming (Wing et al. 2020).
42 While the radiative feedbacks associated with tropical convection remain difficult to constrain,
43 recent work has advanced understanding of how warming may impact more specific aspects of
44 convection, including its large-scale organization (e.g., Coppin and Bony 2018), precipitation
45 efficiency (e.g., Lutsko and Cronin 2018), and anvil cloud evolution (e.g., Gasparini et al. 2021).
46 In this paper, we examine how warming may impact the mean profile of cloud ice amount.

47 The radiative-convective equilibrium (RCE) approximation provides a conceptual link between
48 the formation of ice and the atmospheric radiative cooling rate Q_R . The formation of ice during
49 convection releases latent heat, which is transported to the upper troposphere (UT) by deep
50 convective plumes. This latent heating, along with the eddy heat flux convergence associated with
51 the convection, constitutes the total convective heating. In RCE, convective heating is balanced by
52 Q_R , which we can compute accurately for known temperature and moisture profiles.

53 Models of varying complexity predict that Q_R in the UT will increase with warming if the
54 temperature profile approximately follows a moist adiabat. This result is supported by prior
55 work using early general circulation models (Mitchell and Ingram 1992; Knutson and Manabe
56 1995), simple spectral models (Jeevanjee and Fueglistaler 2020), and modern line-by-line models
57 (Jeevanjee and Fueglistaler 2020). Jeevanjee and Romps (2018) showed that the radiative flux
58 divergence ($\text{W/m}^2/\text{K}$ in temperature coordinates) at any particular temperature is unaffected by
59 surface warming in simulations of RCE. But warming drives isotherms to lower pressures, where
60 the ambient air is less dense. This produces an increase in Q_R (K/day), which is inversely related
61 to density. Hartmann et al. (2021) used the cooling-to-space approximation to show that emission
62 from the atmosphere is purely a function of temperature and relative humidity, but as the surface
63 warms and the emission moves to a lower pressure, the transmission to space increases, which
64 allows Q_R to increase. If the temperature profile follows a moist adiabat, Q_R preferentially increases
65 at the anvil cloud level, causing the Q_R profile to become more top-heavy.

66 This paper seeks to understand how the warming-driven increase in Q_R affects the mean profile
67 of cloud ice amount in an RCE framework. Doing so requires us to examine the connection
68 between radiative cooling, latent heating, and the ice mass mixing ratio q_i in the UT. In section
69 2, we describe a set of CRM simulations that allow us to examine how the atmosphere responds
70 to an increase in Q_R with and without a corresponding change in surface temperature. This will

71 show that the q_i response to warming is tempered by an increase in the efficiency by which ice
72 imparts latent heat to the UT. To understand this change, we develop a mathematical expression for
73 the ice-related latent heating rate and use it to diagnose the CRM results (sections 3 and 4). This
74 will show that the increased efficiency of latent heating is caused by the migration of isotherms
75 to lower pressures and by the slight warming of the top of the convective layer. We discuss and
76 contextualize these results in section 5.

77 **2. Cloud-Resolving Model Simulations**

78 We conduct RCE simulations using the System for Atmospheric Modeling (SAM; Khairoutdinov
79 and Randall 2003) with RRTM radiative transfer code (Iacono et al. 2000; Mlawer et al. 1997). The
80 model domain is $96 \text{ km} \times 96 \text{ km}$ with 2-km horizontal resolution and periodic lateral boundaries.
81 Because this small domain precludes convective aggregation, we can be confident that changes
82 in the degree of aggregation do not impact our results. The vertical grid has 128 levels with
83 variable spacing. The spacing is 50 m near the surface, smoothly increases to $\sim 300 \text{ m}$ by 5 km,
84 and increases again between 25 and 39 km to a maximum spacing of 1 km. Gravity waves are
85 dampened by a sponge layer extending upward from 27 km. Sea surface temperature (SST) is fixed
86 and uniform, there is no rotation, and insolation follows a fixed diurnal cycle corresponding to
87 January 1 at the equator. We use the Predicted Particle Properties (P3) bulk microphysics scheme
88 (Morrison and Milbrandt 2015), which has a single ice-phase hydrometeor category with four
89 prognosed variables: total ice mass, total ice number, rime mass, and rime volume. Because P3
90 has only one ice category, we do not differentiate between precipitating and nonprecipitating ice.
91 We use the term “cloud ice” to refer to all ice-phase hydrometeors and the symbol q_i to denote the
92 total ice mass mixing ratio.

93 Three simulations are conducted:

- 94 1. *con300*: 350-day control run with 300-K SST
- 95 2. *con305*: 350-day warming run with 305-K SST
- 96 3. *force300*: experimental run with 300-K SST and a forced cooling F intended to mimic the
97 upper tropospheric Q_R response to warming. This run is branched from *con300* at day 150
98 and integrated for another 150 days. F is sinusoidal in pressure coordinates with positive
99 (cooling) and negative (warming) lobes between 250-550 and 550-850 hPa, respectively, and
100 a maximum amplitude of 0.26 K/day (Fig. 1a). Because of its sinusoidal structure, F has
101 a mass integral of zero and thus no direct effect on the column-integrated cooling rate. We
102 conducted an additional run in which F consisted only of its upper lobe, but there were no
103 significant differences in the upper tropospheric quantities of interest.

104 The time-averaged results shown in the following sections reflect the last 75 days of each model
105 run.

106 In equilibrium, the convective heating rate must balance the sum of Q_R and F , which we denote
107 as Q_{R+F} . The solid lines in Fig. 1b-c show Q_{R+F} for each run. Because there is no forcing in
108 *con300* and *con305*, Q_{R+F} is just equal to Q_R in those runs and is larger in *con305* for the reasons
109 discussed in section 1. The increase in Q_R with warming is limited to temperatures above ~ 220
110 K, since the Q_R profile is constrained to decrease at colder temperatures due to the scarcity of
111 water vapor (Hartmann and Larson 2002). In *force300*, Q_R (dashed red line) is similar to that in
112 *con300*, reflecting the fact that the two runs have equal SST and thus very similar temperature and
113 moisture profiles. But because F is nonzero in *force300*, upper tropospheric Q_{R+F} is more like that
114 in *con305*, especially when viewed in temperature coordinates (Fig. 1c). So while the temperature,
115 moisture, and Q_R profiles in *force300* match its 300-K SST, the total cooling “experienced” in the
116 UT corresponds to a SST of 305 K. This is exactly the intent of the temperature forcing and will

117 allow us to compare the atmosphere’s response to increased Q_{R+F} in the presence and absence of
118 SST warming. An implication of this approach is that F does not capture the warming-driven shift
119 of the Q_R profile to lower pressures (Fig 1b).

120 The increase in upper tropospheric Q_{R+F} in con305 and force300 must be balanced by an increase
121 in convective heating. We can examine the energy budget of the UT to better understand how this
122 is achieved. The thermodynamic variable used for this budget analysis and throughout the rest of
123 the paper is the liquid-ice static energy:

$$s = c_p T + gz - Lq_l - L_s q_i. \quad (1)$$

124 C_p is the specific heat of dry air at constant pressure, T is temperature, g is the gravitational
125 acceleration, q_l is the mass mixing ratio of all liquid condensate, and L and L_s are the latent heats
126 of vaporization and sublimation, respectively. s is the prognostic thermodynamic variable in SAM
127 and is exactly conserved by the model’s governing equations. It is informative to use s for our
128 analysis because it is approximately conserved during moist adiabatic processes and is therefore
129 unaffected by phase changes.

130 Fig. 2a shows the model-computed tendencies of s due to Q_{R+F} , advection, and latent heating.
131 These three tendencies, along with a very small diffusive tendency (not shown), form a closed
132 energy budget. The advective tendency is negative because s increases with height, meaning that
133 convective plumes deposit low- s air from the surface into the high- s UT. Because there is no
134 large-scale vertical motion in these runs, the advective tendency is comprised solely of the heating
135 by resolved eddies. The convective heating rate is thus equal to the sum of the advective and latent
136 heating tendencies.

137 Fig. 2a indicates that both the latent and advective components of the s budget strengthen in
138 response to the increase in Q_{R+F} in con305 and force300. The increase in latent heating dominates,

139 so the convective heating rate increases as a result. This increase in latent heating must be associated
 140 with changes in ice, since liquid condensate is scarce or nonexistent at temperatures below ~ 245
 141 K. To formally distinguish the ice-related latent heating from the total latent heating, we define \dot{s}_{ice}
 142 as the latent heating tendency of s due to ice alone. To better conceptualize \dot{s}_{ice} , let us consider
 143 a saturated air parcel rising in a deep convective plume. Once the freezing level is surpassed, ice
 144 accumulates via freezing, vapor deposition, and/or new nucleation. This releases latent heat, which
 145 warms the parcel but does not change s , since s is conserved during phase changes. For as long as
 146 the ice remains with the parcel, there is the possibility that it sublimates and consumes the latent
 147 heat released during its formation. But if the ice sediments out of the parcel, that latent heat is
 148 irreversibly left behind, and by Eq. (1), s increases because q_i has decreased. The important point
 149 here is that the latent heating of s results not from the formation of ice but from its irreversible
 150 sedimentation later on. This can be expressed mathematically as

$$\dot{s}_{ice} = -L_s \dot{q}_{i_{sed}} \quad (2)$$

151 where $\dot{q}_{i_{sed}}$ is the tendency of q_i due to sedimentation.

152 Because \dot{s}_{ice} is determined by the net ice sedimentation rate rather than q_i itself, the relative
 153 differences in \dot{s}_{ice} between the three simulations are not necessarily reflected in their domain-
 154 averaged q_i profiles. This is evident in Figure 2b. q_i is highest in force300 despite the fact that
 155 there is more latent heating in con305 over much of the same temperature range. In con305, the
 156 fractional increase in \dot{s}_{ice} relative to con300 far exceeds that in q_i throughout most of the UT. In
 157 force300, while the fractional changes in \dot{s}_{ice} and q_i are not exactly equal, they are much more
 158 similar. This difference is encapsulated by what we define as the latent heating efficiency:

$$\epsilon \equiv \frac{\dot{s}_{ice}}{L_s q_i}. \quad (3)$$

159 It is important that ϵ not be confused with the precipitation efficiency, as they are very different in
160 nature. As ϵ increases, a smaller mean q_i is needed to achieve a given amount of latent heating.
161 Fig. 2c shows profiles of ϵ for the three simulations. At air temperatures exceeding 215 K, ϵ is
162 nearly the same in con300 and force300 but is larger in con305, suggesting that ϵ increases with
163 SST. As will be shown later, additional simulations with SSTs of 295, 310, and 315 K support this
164 trend.

165 Changes in the domain-averaged q_i can be caused both by changes in cloud fraction and by
166 changes in the in-cloud ice amount. These two factors have important implications for both the
167 top-of-atmosphere energy budget and atmospheric radiative heating rates, which have been shown
168 to play an important role in the circulation response to warming (Voigt et al. 2019). In con305,
169 ice cloud fraction is lower at any particular temperature than in con300 but the in-cloud q_i is
170 higher on average (Fig. 3). The fractional increase in in-cloud q_i dominates the decrease in
171 cloud fraction for $T > 224$ K, and so the the domain-averaged q_i increases there. This results
172 primarily from an increase in the amount of ice within deep convective cores; if we were to exclude
173 the 2% of the model domain with the highest column-integrated ice water path (IWP) from the
174 calculation of domain-averaged q_i , then q_i would actually decrease with warming at most upper
175 tropospheric temperature levels. Thus, it is the increase in q_i in the iciest parts of the atmosphere
176 that is responsible for the increase in domain-averaged q_i at fixed temperature. In contrast, the
177 large increase in domain-averaged q_i in force300 comes mostly from an increase in cloud fraction,
178 with a small increase in in-cloud q_i playing a lesser role. These differences make sense: as SSTs
179 warm, the troposphere deepens and warms at its base, and convective updrafts accumulate a greater
180 amount of condensate before reaching any particular isotherm in the upper troposphere. Because
181 there is no warming in force300, any significant increase in domain-averaged q_i must come from
182 changes in cloud fraction.

183 Cloud changes can be further understood by examining the probability density functions (PDFs)
 184 of IWP, shown in Fig. 4a. The PDFs are computed from instantaneous 2D snapshots taken at
 185 6-hour intervals for the final 75 days of each simulation. None of these snapshots contain grid cells
 186 with zero IWP, likely because the domain is relatively small and is easily covered by ice spreading
 187 out from convective regions. Because true clear-sky conditions do not occur, altering the IWP
 188 distribution is a zero-sum game: differences in the PDFs at one IWP must be compensated for by
 189 differences at another IWP rather than by differences in the total cloud coverage. In con305, SST
 190 warming reduces the coverage of clouds with \log_{10} IWP between -0.3 and 3.5 (Fig. 4b), which
 191 include convective cores, detrained anvil clouds, and other thin cirrus (Sokol and Hartmann 2020).
 192 This reduction is compensated for by an increase in the area with \log_{10} IWP between -2 and -0.3,
 193 which is as close as it gets to clear-sky conditions in these simulations. In essence, warming shifts
 194 the IWP distribution towards lower values, and the mean IWP decreases by 6% as a result (Fig.
 195 4a). This may seem counterintuitive given the increase in domain-averaged q_i at fixed temperature
 196 shown in Fig. 2b, but the pressure and density at a fixed temperature decrease with SST warming,
 197 and so the same q_i (kg/kg) corresponds to a smaller ice water content (kg/m^3), which is the quantity
 198 used to compute IWP. In force300, the IWP changes are reversed. The frequency of high IWPs
 199 increases at the expense of low IWPs, which shifts the distribution towards higher values and
 200 increasing the mean IWP by 23%.

201 In this brief overview of the CRM results, we have found that RCE requires \dot{s}_{ice} to increase in
 202 response to an increase in Q_{R+F} whether it is driven by SST warming or an imposed temperature
 203 forcing. On the other hand, ϵ is largely unaffected by the temperature forcing but increases
 204 with warming. This allows the q_i profiles in con305 and force300 to differ substantially even at
 205 temperatures where \dot{s}_{ice} is equal. In con305, an increase in convective core q_i drives the slight
 206 increase in domain-averaged q_i , while in force300 the much larger increase in domain-averaged

207 q_i is due mainly to greater cloudiness. These results raise some interesting questions. What is the
 208 relationship between latent heating and q_i ? Why does ϵ increase with SST? And what can this tell
 209 us about the q_i response to warming? We address these questions in the following sections.

210 3. A Theoretical Model for Latent Heating

211 Our goal in this section is to develop an expression relating \dot{s}_{ice} to q_i . Eq. (2) defines \dot{s}_{ice} in
 212 terms of $\dot{q}_{i_{sed}}$, which is the sedimentation tendency of q_i equal to

$$\dot{q}_{i_{sed}} = -\frac{1}{\rho} \frac{\partial F_{sed}}{\partial z} \quad (4)$$

213 where ρ is the air density and F_{sed} is the sedimentation ice flux. In the P3 scheme, this is given by

$$F_{sed} = \rho q_i f V_m \quad (5)$$

214 where V_m is the mass-weighted ice crystal terminal fall speed calculated following Mitchell and
 215 Heymsfield (2005). f is an air density modification to V_m which, following Heymsfield et al.
 216 (2007), is given by $(\rho_0/\rho)^{0.54}$, where ρ_0 is a reference density. Substituting in for f in (5) gives

217 $F_{sed} = \rho_0^{0.54} \rho^{0.46} q_i V_m$. Combining this with (2) and (4) yields

$$\dot{s}_{ice} = \frac{k}{\rho} \frac{\partial}{\partial z} \left(\rho^{0.46} q_i V_m \right) \quad (6)$$

218 where $k = L_s \rho_0^{0.54}$. Expanding the derivative gives

$$\dot{s}_{ice} = \frac{k}{\rho^{0.54}} \left(0.46 q_i V_m \frac{\partial \ln \rho}{\partial z} + q_i \frac{\partial V_m}{\partial z} + V_m \frac{\partial q_i}{\partial z} \right). \quad (7)$$

219 Using the ideal gas law $p = \rho R_d T_v$ and hydrostatic balance $\partial p / \partial z = -\rho g$, it can be shown that

$$\frac{\partial \ln \rho}{\partial z} \approx \frac{1}{T} \left(\Gamma - \frac{g}{R_d} \right) \quad (8)$$

220 where Γ is the lapse rate and R_d the gas constant for dry air. Here we have assumed that the virtual
 221 temperature T_v is approximately equal to the absolute temperature T , which is a good approximation

222 over the range of temperatures that we will consider. Combining (7) and (8) and replacing $\partial/\partial z$
 223 with $-\Gamma \cdot \partial/\partial T$ gives

$$\dot{s}_{ice} = \frac{k}{\rho^{0.54}} \left[\Gamma \left(\frac{0.46V_m q_i}{T} - q_i \frac{\partial V_m}{\partial T} - V_m \frac{\partial q_i}{\partial T} \right) - \frac{0.46c q_i V_m}{T} \right] \quad (9)$$

224 where $c = g/R_d$. The conversion to temperature coordinates simplifies the comparison of sim-
 225 ulations with different SSTs because the temperature at which Q_R falls towards zero—which is
 226 also the top of the convective layer—is approximately fixed (Hartmann and Larson 2002). This is
 227 illustrated in Fig. 1c, in which the Q_R and Q_{R+F} curves collapse onto one another at ~ 220 K.

228 Eq. (9) is useful because it allows us to calculate the domain-averaged \dot{s}_{ice} profile given profiles
 229 of T , ρ , q_i , and V_m . If we convert these profiles to temperature coordinates, we can calculate
 230 $\partial q_i/\partial T$ and $\partial V_m/\partial T$, which we denote as q'_i and V'_m , respectively. Then, using the total differential
 231 of (9), we can attribute changes in \dot{s}_{ice} at some fixed T to changes in six different variables:

$$\Delta \dot{s}_{ice} \approx \Delta \rho \frac{\partial \dot{s}_{ice}}{\partial \rho} + \Delta \Gamma \frac{\partial \dot{s}_{ice}}{\partial \Gamma} + \Delta V_m \frac{\partial \dot{s}_{ice}}{\partial V_m} + \Delta V'_m \frac{\partial \dot{s}_{ice}}{\partial V'_m} + \Delta q_i \frac{\partial \dot{s}_{ice}}{\partial q_i} + \Delta q'_i \frac{\partial \dot{s}_{ice}}{\partial q'_i}. \quad (10)$$

232 Here, ΔX denotes the change in X at fixed T relative to some baseline. Expressions for the partial
 233 derivatives can be determined analytically from (9) and are provided in appendix A. Eq. (10) is an
 234 accurate approximation of $\Delta \dot{s}_{ice}$ over the range of atmospheric states produced by the three model
 235 runs (appendix B).

236 4. Application to Model Simulations

237 We can now use Eq. (10) to understand the differences in \dot{s}_{ice} between the three simulations. To
 238 do so, we must evaluate each term on the right hand side for con305 and force300, using con300 as
 239 a baseline. The value of each term can be interpreted as the contribution of that variable to the total
 240 change in \dot{s}_{ice} at some particular T . The model provides hourly profiles of domain-averaged T , ρ ,
 241 q_i , and F_{sed} in height coordinates. For each time step, we compute Γ and compute the q_i -weighted

242 V_m as $F_{sed}/(f\rho q_i)$, which follows from Eq. (5). We then convert the vertical grid to temperature
 243 coordinates using the time- and domain-averaged T at each vertical level, interpolate the profiles
 244 onto a common T grid, and calculate q'_i and V'_m . We use output from con300 to compute the partial
 245 derivatives in Eq. (10), and the Δ terms are computed for con305 and force300 with respect to
 246 con300.

247 Fig. 5 shows the results of this procedure, with each colored line representing one of the six
 248 terms on the right hand side of Eq. (10). The bold black lines, which show $\Delta\dot{s}_{ice}$, are equal to
 249 the sum of the six individual terms and correspond closely to the differences in the latent heating
 250 profiles shown in Fig. 2a. The profiles have been normalized by C_p so that they are in K/day. If
 251 a profile is near the zero line, then the variable it represents does not change significantly at that T
 252 and therefore has little impact on \dot{s}_{ice} .

253 In the following sections, we discuss each variable and its relevance to changes in \dot{s}_{ice} before
 254 synthesizing the results with a discussion of latent heating efficiency. All changes (e.g., increases
 255 and decreases) mentioned in this section are with respect to con300 unless stated otherwise. It is
 256 important to remember that \dot{s}_{ice} is only equal to the total latent heating of s when the effects of
 257 liquid condensate are negligible. In our model runs, \dot{s}_{ice} accounts for 90% or more of the total
 258 latent heating at temperatures colder than 245 K, and we therefore restrict our analysis to that range.

259 *a. Density and Lapse Rate*

260 We begin by discussing ρ and Γ together because their values at any particular T are both
 261 fundamentally linked to SST. This linkage arises from the fact that the tropical temperature profile
 262 is dynamically constrained to be close to a moist adiabat originating from the boundary layer (Sobel
 263 et al. 2001), and the temperature of the boundary layer is determined by the SST. Since con300 and
 264 force300 have the same SST, they also have similar T profiles and therefore similar ρ and Γ at any

265 particular T . Consequently, in force300 the ρ and Γ contributions to $\Delta\dot{s}_{ice}$ (blue and orange lines
266 in Fig. 5b, respectively) are negligible.

267 On the other hand, SST warming in con305 drives isotherms upwards toward lower pressures,
268 and the ρ at any particular T decreases as a result. Since \dot{s}_{ice} and ρ are inversely related in Eq. (9),
269 the decrease in ρ acts to increase \dot{s}_{ice} , as evidenced by the positive values of the ρ term (blue line)
270 in Fig. 5a. The physical interpretation of this ρ effect is straightforward: ice crystals fall faster at
271 lower air densities because drag is reduced. As ρ decreases, ice crystals are quick to sediment out
272 of a parcel and leave their latent heat behind. Mathematically, the ρ effect stems from the density
273 modification f applied to the ice crystal fall speed, and the magnitude of the ρ effect is therefore
274 sensitive to the formulation of f . But insofar as ρ and fall speed are inversely related, the sign of
275 the ρ effect is robust.

276 Changes in Γ in con305 act to reduce \dot{s}_{ice} , as shown by the orange line in Fig. 5a. This, too,
277 arises from the migration of isotherms to lower pressures with warming, which reduces the moist
278 adiabatic lapse rate at any particular T . The pressure dependence of the moist adiabatic lapse
279 rate is indirect, occurring by way of the saturation specific humidity. The reduction in Γ with
280 warming causes our temperature range of interest to expand vertically in Cartesian space, which
281 “stretches out“ and weakens the sedimentation flux divergence, reducing \dot{s}_{ice} . The sign of the Γ
282 effect seems robust considering that an increase in static stability (decrease in Γ) with warming
283 has long appeared in observations and models (Knutson and Manabe 1995; Zelinka and Hartmann
284 2010, 2011; Bony et al. 2016). It’s magnitude, especially in the uppermost UT, could be influenced
285 by the model’s representation of ozone. Γ could also be sensitive to model resolution if resolution
286 impacts the entrainment rate, since entrainment modifies the RCE temperature profile (Zhou and
287 Xie 2019).

288 The arguments in this section, grounded in first principles, tell us that the ρ and Γ effects
289 push \dot{s}_{ice} in opposing directions as SST warms. Ice crystals fall faster but must travel a greater
290 distance from one isotherm to the next. The combined effect of ρ and Γ , which is relatively
291 small compared to their individual effects, is negative at temperatures below 220 K and positive
292 at warmer temperatures, with a positive mass integral between 220 and 245 K. Thus, if all else is
293 equal, warming causes the \dot{s}_{ice} profile to increase in magnitude and shift slightly towards warmer
294 temperatures.

295 *b. Ice Crystal Fall Speed*

296 We turn now to V_m and V'_m . Unlike ρ and Γ , V_m and V'_m do not have an obvious SST dependence
297 that can be inferred from first principles, so we instead rely here on their prediction by the P3
298 microphysics scheme. In P3, V_m is determined following Mitchell and Heymsfield (2005) and
299 depends on several microphysical quantities, including ice particle density. Ice density is predicted
300 from the scheme's prognostic ice variables and accounts for the effects of riming, which is critical for
301 the simulation of certain convective structures (Morrison et al. 2015). This makes P3 well suited
302 for the present analysis compared to schemes that sort ice particles into predefined categories
303 with prescribed fall speeds. Changes in V_m between the three simulations reflect changes in ice
304 microphysics and do not necessarily correspond to changes in the *actual* fall speed, since we have
305 separated V_m from its air density modification factor f .

306 In force300, the V_m and V'_m effects on \dot{s}_{ice} (purple and brown lines in Fig. 5b, respectively) are
307 negligible, indicating that changes in ice microphysical properties cannot explain the increase in
308 latent heating. In con305, the V_m and V'_m effects are large enough to warrant discussion but are
309 still relatively small compared to the other terms. V_m increases (becomes less negative) throughout
310 the UT, which acts to reduce \dot{s}_{ice} above the level of maximum q_i (234 K) and enhance \dot{s}_{ice} below.

311 The V'_m effect has a more complicated vertical structure and is largest between 235-240 K, where
312 a steepening of the V_m profile strengthens the sedimentation flux divergence and enhances \dot{s}_{ice} .

313 Understanding the slight differences in V_m and V'_m between our three simulations requires an in-
314 depth analysis of their microphysics. We forgo such analysis here, since the V_m and V'_m effects are
315 relatively small in both con305 and force300, and neglecting them produces only minor changes in
316 $\Delta\dot{s}_{ice}$. Moreover, the insights gained from such an analysis would be specific to the P3 microphysics
317 scheme and the V_m parameterization it employs. The parameterization of V_m is an obvious source
318 of uncertainty in our results, and while the small size of the V_m and V'_m effects alleviates some
319 of this uncertainty, it is possible that a different fall speed parameterization could produce very
320 different results, although this would likely require large microphysical changes. The importance
321 of ice fall speed in the tropical energy budget—underscored by the mere presence of V_m and V'_m in
322 Eq. (9) and by a large body of research (e.g., Grabowski et al. 2000; Mitchell et al. 2008; Sanderson
323 et al. 2008)—is worthy of further study.

324 *c. Cloud Ice*

325 The two remaining terms in Eq. 10 are the q_i and q'_i terms, shown respectively by the green
326 and red lines in Fig. 5. In force300, the increase in q_i acts to increase \dot{s}_{ice} at all T . The q_i effect
327 is largest at warmer temperatures, where the absolute change in q_i is greatest and where \dot{s}_{ice} is
328 especially sensitive to changes in q_i because V_m is large. The q'_i effect is also significant in force300
329 and reflects a general steepening of the q_i profile, which causes q'_i at any particular T to increase
330 in magnitude but retain the same sign. If all else is equal, this acts to enhance latent heating above
331 the level of maximum q_i and hinder it below. The q'_i effect dominates the total change in \dot{s}_{ice} at
332 cold temperatures, whereas the q_i effect dominates at warmer temperatures.

333 In con305, the q_i and q'_i effects have a more complex vertical structure. For reasons outlined by
 334 Zelinka and Hartmann (2010), the top of the convective layer warms by about ~ 1 K in response to
 335 the SST increase. The upper extent of the q_i profile shows a similar warming, but the lower extent
 336 is tied to the freezing level and thus does not warm in the same way. As a result, the q_i profile is
 337 vertically squashed in temperature space towards warmer temperatures. One consequence of this
 338 shift is that the q_i and q'_i effects are both negative at low T . Between 215-225 K, the q'_i effect
 339 increases rapidly with T and becomes larger in magnitude than the q_i effect, which is still negative.
 340 This is significant because it produces an increase in \dot{s}_{ice} despite a decrease in the amount of ice.
 341 The q'_i effect has the largest magnitude of any term in con305 throughout much of the UT and
 342 at some points is even larger than its counterpart in force300. At ~ 239 K, the q_i , q'_i , ρ , and V'_m
 343 effects all contribute equally to the increase in \dot{s}_{ice} in con305. This is in stark contrast to force300,
 344 in which only the q_i and q'_i effects are significant. This has important implications for the latent
 345 heating efficiency, which is discussed in the next section.

346 *d. Latent Heating Efficiency*

347 Having examined how \dot{s}_{ice} changes in response to warming SSTs and an imposed forcing, we
 348 can return to the question posed at the end of section 2: why does the latent heating efficiency ϵ
 349 increase with SST, and what can this tell us about the q_i response to warming? Just as we did with
 350 \dot{s}_{ice} , we can decompose changes in ϵ into contributions from the same six variables (appendix A).
 351 This decomposition is shown in Fig. 6, which is restricted to the 215-245 K range over which ϵ
 352 shows a clear dependency on SST. The ρ , Γ , V_m , and V'_m contributions have been grouped into a
 353 single "non- q_i " term. These non- q_i terms and q'_i have straightforward effects on ϵ : wherever they
 354 act to increase (decrease) \dot{s}_{ice} , they also act to increase (decrease) ϵ . The q_i effect on ϵ is more
 355 complicated, since q_i appears both explicitly and implicitly (via \dot{s}_{ice}) in Eq. (3). It can be shown

356 from (3) that

$$\frac{\partial \epsilon}{\partial q_i} = \frac{1}{L_s q_i^2} (q_i \frac{\partial \dot{s}_{ice}}{\partial q_i} - \dot{s}_{ice}) = \frac{k \Gamma V_m q_i'}{L_s \rho^{0.54} q_i^2} \quad (11)$$

357 The algebraic signs on the right hand side work out such that $\partial \epsilon / \partial q_i$ takes the opposite sign of
358 q_i' . Above the q_i maximum at 234 K, q_i' is positive and so $\partial \epsilon / \partial q_i$ is negative, meaning that ϵ will
359 decrease in response to an increase in cloud ice.

360 In force300, the total change in ϵ (solid black line in Fig. 6b) is relatively small. Since the
361 non- q_i contribution is also small, it must then be the case that the q_i (green line) and q_i' (red line)
362 effects approximately cancel. Indeed, throughout most of the temperature range shown in Fig. 6,
363 the decrease in ϵ associated with enhanced q_i is balanced by the increase associated with steeper
364 q_i gradients.

365 On the other hand, ϵ increases significantly in con305. The non- q_i terms account for approxi-
366 mately half of the ϵ increase at high T but work against the increase at colder T . The rest of the
367 ϵ change is explained by the q_i and q_i' effects, which differ significantly in shape from those in
368 force300 because of the slight warming of the top of the q_i profile. To examine this effect, we
369 shifted the con305 q_i profile towards colder temperatures by 1 K, which brings the top of the profile
370 in line with that from con300. We then recalculated q_i' and ϵ at each T . The dotted black line in
371 Fig. 6a shows the resulting $\Delta \epsilon$ profile, which is reduced in magnitude by $\sim 50\%$ or more compared
372 to the actual con305 profile. This shows that approximately half of the ϵ increase in the UT can be
373 explained by the warming of the convective layer top. At warmer temperatures, the non- q_i terms
374 and warming of the convective layer top account for nearly all of the increase in ϵ from con300
375 to con305. At cold temperatures, where the non- q_i terms work against the ϵ increase, the rest is
376 accounted for by the portions of the q_i and q_i' effects that are not associated with the temperature
377 at the top of the convective layer.

378 The increase in ϵ with warming can be understood physically as a shortening of the residence time
379 of ice at some particular temperature against sedimentation. This residence time can be expressed
380 as $\tau_{sed} = -q_i / \dot{q}_{i_{sed}}$, where the negative sign converts the sedimentation tendency to a removal rate.
381 Using Eqs. (3) and (2), it can be shown that $\tau_{sed} = \epsilon^{-1}$. When ϵ is high as in con305, ice is cycled
382 through the upper troposphere at a faster rate, and the climatological q_i at any particular T is kept
383 low by rapid sedimentation. On the other hand, when ϵ is low, ice lingers at a particular temperature
384 for a greater amount of time before sedimenting onward to the next isotherm, and the same latent
385 heating rate is associated with larger climatological q_i . It is important that this shortening of τ_{sed}
386 with warming not be equated with an increase in the fall speed, which is only one of several factors
387 that determine τ_{sed} .

388 The pattern of increasing ϵ and decreasing τ_{sed} with warming is supported by three additional
389 model runs with SSTs of 295, 310, and 315 K, as shown in Fig. 7. Apart from their SSTs, these
390 three runs have identical setups to con300 and con305.

391 5. Summary and Discussion

392 This paper is motivated by the question of how the mean q_i in the tropical UT would respond to
393 an increase in the radiative cooling rate. In our RCE simulations, the q_i response to warming SSTs
394 is tempered by an increase in the latent heating efficiency ϵ , which allows con305 and force300
395 to achieve the same latent heating rate with different amounts of ice. The theoretical model
396 developed in section 3 reveals that q_i is only one of several factors that determine \dot{s}_{ice} and therefore
397 ϵ . Applying this model to our simulations, we found that the increase in ϵ with warming can be
398 explained primarily by 1) changes in the non- q_i terms and 2) the slight warming of the upper branch
399 of the q_i profile. Another way to understand these results is that ice is cycled across isotherms at a
400 faster rate in con305 than in force300, and the lingering of ice at an isotherm in force300 results in a

401 larger climatological q_i for a given latent heating rate. These results are summarized schematically
402 in Fig. 8.

403 An important limitation of this work is that we have used only one model with one cloud
404 microphysics scheme. Given the wide variety of cloud condensate profiles produced by the CRMs
405 participating in RCEMIP (see Fig. 10c in Wing et al. 2020), it is likely that the q_i response to
406 warming varies considerably across models. But our finding that ϵ increases with warming relies
407 on some basic mechanisms that are widely supported by previous work, namely that SST warming
408 causes a slight warming of the convective layer top and a decrease in ρ and Γ at fixed T . Barring
409 drastic intermodel differences in the V_m response to warming, it is reasonable to suspect that the
410 increase in ϵ with warming is robust. It would be beneficial to assess whether the RCEMIP models
411 agree in this regard.

412 In this study, we have focused primarily on changes in the *domain-averaged* q_i because it can
413 be theoretically linked to the energy balance requirements of RCE, as we have shown. But when
414 it comes to global climate, changes in cloud amount and cloud optical properties with warming
415 are of primary importance. In our RCE simulations, warming SSTs cause a reduction in cloud
416 fraction and an increase in mean in-cloud q_i at fixed temperature (Fig. 3). Decreasing ice cloud
417 area is consistent with the long-debated iris hypothesis (Lindzen et al. 2001) and the more recently
418 developed stability iris hypothesis (Bony et al. 2016), both of which predict a reduction in anvil
419 cloud fraction with warming. It is also in agreement with the majority of the cloud-resolving
420 models in the RCEMIP ensemble (Wing et al. 2020). But it is important to recognize that a
421 reduction in high cloud fraction is *not* an inevitable consequence of an increase in ϵ or an increase
422 in mean q_i . By themselves, increases in ϵ and q_i do not imply any specific changes in cloud amount
423 or optical properties; because deep convection is associated with a variety of cloud types, there
424 are myriad ways by which increases in ϵ and mean q_i could be achieved. The link between mean

425 q_i and cloud fraction is further complicated by, among other factors, warming-induced changes in
 426 convective organization (Emanuel et al. 2014; Wing et al. 2017; Coppin and Bony 2018; Cronin
 427 and Wing 2017) and the complexity of anvil cloud dynamics (Schmidt and Garrett 2013; Hartmann
 428 et al. 2018; Gasparini et al. 2019; Wall et al. 2020). Future work may focus on the extension of the
 429 framework developed here to three dimensions, which would reveal how changes in the mean ice
 430 amount and latent heating efficiency are manifested across the distribution of convective clouds.

431 *Acknowledgments.* We acknowledge Peter Blossey and Blaž Gasparini for their help with the
 432 SAM model code. We thank Aiko Voigt and two anonymous reviewers for their constructive
 433 comments. This work was supported by NSF grant AGS-1549579. ABS is supported by NASA
 434 FINESST grant 80NSSC20K1613.

435 *Data availability statement.* Output files from the model runs used in this study are available at
 436 <http://hdl.handle.net/1773/46946>. The model source code is publicly available.

437 APPENDIX A

438 Analytical Expressions for the Sensitivity of \dot{s}_{ice} and ϵ

439 Here we provide expressions for the partial derivatives of \dot{s}_{ice} on the right hand side of Eq. (10).
 440 These expressions are derived from Eq. (9) and used to construct the curves shown in Fig. 3. q'_i
 441 and V'_m denote $\partial q_i / \partial T$ and $\partial V_m / \partial T$, respectively. As an approximation, q_i and q'_i are treated as
 442 independent of one another, as are V_m and V'_m .

$$\frac{\partial \dot{s}_{ice}}{\partial \rho} = -0.54 \frac{\dot{s}_{ice}}{\rho}$$

$$\frac{\partial \dot{s}_{ice}}{\partial \Gamma} = \frac{k}{\rho^{0.54}} \left(\frac{0.46 V_m q_i}{T} - q_i V'_m - V_m q'_i \right)$$

$$\frac{\partial \dot{s}_{ice}}{\partial q_i} = \frac{k}{\rho^{0.54}} \left[\Gamma \left(\frac{0.46V_m}{T} - V'_m \right) - \frac{0.46cV_m}{T} \right]$$

$$\frac{\partial \dot{s}_{ice}}{\partial q'_i} = -\frac{kV_m\Gamma}{\rho^{0.54}}$$

$$\frac{\partial \dot{s}_{ice}}{\partial V_m} = \frac{k}{\rho^{0.54}} \left[\Gamma \left(\frac{0.46q_i}{T} - q'_i \right) - \frac{0.46cq_i}{T} \right]$$

$$\frac{\partial \dot{s}_{ice}}{\partial V'_m} = -\frac{kq_i\Gamma}{\rho^{0.54}}$$

443 In section 4d, $\Delta\epsilon$ is decomposed in the same manner as $\Delta\dot{s}_{ice}$. The total differential approximation
 444 for $\Delta\epsilon$, analogous to equation (10), is

$$\Delta\epsilon \approx \Delta\rho \frac{\partial\epsilon}{\partial\rho} + \Delta\Gamma \frac{\partial\epsilon}{\partial\Gamma} + \Delta V_m \frac{\partial\epsilon}{\partial V_m} + \Delta V'_m \frac{\partial\epsilon}{\partial V'_m} + \Delta q_i \frac{\partial\epsilon}{\partial q_i} + \Delta q'_i \frac{\partial\epsilon}{\partial q'_i}.$$

445 Using Eq. 3, $\partial\epsilon/\partial X$ can be expressed in terms of $\partial\dot{s}_{ice}/\partial X$ and evaluated using the expressions
 446 above, where X is ρ , Γ , q_i , q'_i , V_m , or V'_m . The results are used to construct the curves shown in
 447 Fig. 6.

448 APPENDIX B

449 Validation for the Total Differential Approximation for $\Delta\dot{s}_{ice}$

450 Here we validate the use of the total differential to assess changes in \dot{s}_{ice} . Fig. 5 shows $\Delta\dot{s}_{ice}$
 451 (relative to con300) for con305 and force300. The solid lines show the true change, calculated
 452 by evaluating Eq. (9) for each run and taking the difference at each T . Dashed lines show the
 453 approximate change given by the total differential (Eq. 10). For both con305 and force300, the
 454 total differential approximation is within 10% of the true change at all T with the exception of

455 $T < 205$ K, where the fractional errors are slightly larger because $\Delta\dot{s}_{ice}$ is small in magnitude. This
456 close agreement validates the use of the total differential to attribute changes in \dot{s}_{ice} to changes in
457 other factors. The accuracy of the approximation is similar for changes in ϵ (not shown).

458 **References**

459 Bony, S., B. Stevens, D. Coppin, T. Becker, K. A. Reed, A. Voigt, and B. Medeiros, 2016: Ther-
460 modynamic control of anvil cloud amount. *Proceedings of the National Academy of Sciences*,
461 **113** (32), 8927–8932, doi:10.1073/pnas.1601472113.

462 Bony, S., and Coauthors, 2015: Clouds, circulation and climate sensitivity. *Nature Geoscience*,
463 doi:10.1038/ngeo2398.

464 Coppin, D., and S. Bony, 2018: On the Interplay Between Convective Aggregation, Surface
465 Temperature Gradients, and Climate Sensitivity. *Journal of Advances in Modeling Earth Systems*,
466 **10** (12), 3123–3138, doi:10.1029/2018MS001406.

467 Cronin, T. W., and A. A. Wing, 2017: Clouds, Circulation, and Climate Sensitivity in a Radiative-
468 Convective Equilibrium Channel Model. *Journal of Advances in Modeling Earth Systems*, **9** (8),
469 2883–2905, doi:10.1002/2017MS001111, URL <http://doi.wiley.com/10.1002/2017MS001111>.

470 Emanuel, K., A. A. Wing, and E. M. Vincent, 2014: Radiative-convective instability. *Journal of*
471 *Advances in Modeling Earth Systems*, **6** (1), 75–90, doi:<https://doi.org/10.1002/2013MS000270>.

472 Gasparini, B., P. N. Blossey, D. L. Hartmann, G. Lin, and J. Fan, 2019: What Drives the Life Cycle
473 of Tropical Anvil Clouds? *Journal of Advances in Modeling Earth Systems*, **11** (8), 2586–2605,
474 doi:<https://doi.org/10.1029/2019MS001736>.

475 Gasparini, B., P. J. Rasch, D. L. Hartmann, C. J. Wall, and M. Dütsch, 2021: A Lagrangian Perspec-
476 tive on Tropical Anvil Cloud Lifecycle in Present and Future Climate. *Journal of Geophysical*
477 *Research: Atmospheres*, **126** (4), e2020JD033487, doi:<https://doi.org/10.1029/2020JD033487>.

478 Grabowski, W. W., J.-I. Yano, and M. W. Moncrieff, 2000: Cloud Resolving Modeling of Tropical
479 Circulations Driven by Large-Scale SST Gradients. *Journal of the Atmospheric Sciences*, **57** (13),
480 2022–2040, doi:10.1175/1520-0469(2000)057<2022:CRMOTC>2.0.CO;2.

481 Hartmann, D. L., 2016: Tropical anvil clouds and climate sensitivity. *Proceedings of the National*
482 *Academy of Sciences*, **113** (32), 8897–8899, doi:10.1073/pnas.1610455113.

483 Hartmann, D. L., B. D. Dygert, P. N. Blossey, Q. Fu, and A. B. Sokol, 2021: The Vertical Profile
484 of Radiative Cooling in Radiative-Convective Equilibrium: Moist Adiabatic versus Entrainment
485 Modified Plume Model. *Journal of Climate*, **Submitted**.

486 Hartmann, D. L., B. Gasparini, S. E. Berry, and P. N. Blossey, 2018: The Life Cycle and Net
487 Radiative Effect of Tropical Anvil Clouds. *Journal of Advances in Modeling Earth Systems*,
488 **10** (12), 3012–3029, doi:10.1029/2018MS001484.

489 Hartmann, D. L., and K. Larson, 2002: An important constraint on tropical cloud - climate feedback.
490 *Geophysical Research Letters*, **29** (20), 12–1–12–4, doi:<https://doi.org/10.1029/2002GL015835>.

491 Heymsfield, A. J., G.-J. v. Zadelhoff, D. P. Donovan, F. Fabry, R. J. Hogan, and A. J. Illingworth,
492 2007: Refinements to Ice Particle Mass Dimensional and Terminal Velocity Relationships for
493 Ice Clouds. Part II: Evaluation and Parameterizations of Ensemble Ice Particle Sedimentation
494 Velocities. *Journal of the Atmospheric Sciences*, **64** (4), 1068–1088, doi:10.1175/JAS3900.1.

495 Iacono, M. J., E. J. Mlawer, S. A. Clough, and J.-J. Morcrette, 2000: Impact of an improved
496 longwave radiation model, RRTM, on the energy budget and thermodynamic properties of the

497 NCAR community climate model, CCM3. *Journal of Geophysical Research: Atmospheres*,
498 **105 (D11)**, 14 873–14 890, doi:https://doi.org/10.1029/2000JD900091.

499 Jeevanjee, N., and S. Fueglistaler, 2020: Simple spectral models for atmospheric radiative cooling.
500 *Journal of the Atmospheric Sciences*, **77 (2)**, 479–497, doi:10.1175/JAS-D-18-0347.1.

501 Jeevanjee, N., and D. M. Romps, 2018: Mean precipitation change from a deepening troposphere.
502 *Proceedings of the National Academy of Sciences of the United States of America*, **115 (45)**,
503 11 465–11 470, doi:10.1073/pnas.1720683115.

504 Khairoutdinov, M. F., and D. A. Randall, 2003: Cloud Resolving Modeling of the ARM Sum-
505 mer 1997 IOP: Model Formulation, Results, Uncertainties, and Sensitivities. *Journal of the*
506 *Atmospheric Sciences*, **60 (4)**, 607–625, doi:10.1175/1520-0469(2003)060<0607:CRMOTA>
507 2.0.CO;2.

508 Knutson, T. R., and S. Manabe, 1995: Time-Mean Response over the Tropical Pacific to Increased
509 CO₂ in a Coupled Ocean-Atmosphere Model. *Journal of Climate*, **8 (9)**, 2181–2199, doi:10.
510 1175/1520-0442(1995)008<2181:TMROTT>2.0.CO;2.

511 Lindzen, R. S., M. D. Chou, and A. Y. Hou, 2001: Does the Earth Have an Adaptive Infrared
512 Iris? *Bulletin of the American Meteorological Society*, **82 (3)**, doi:10.1175/1520-0477(2001)
513 082<0417:DTEHAA>2.3.CO;2.

514 Lutsko, N. J., and T. W. Cronin, 2018: Increase in Precipitation Efficiency With Surface Warming
515 in Radiative-Convective Equilibrium. *Journal of Advances in Modeling Earth Systems*, **10 (11)**,
516 2992–3010, doi:10.1029/2018MS001482.

517 Mitchell, D. L., and A. J. Heymsfield, 2005: Refinements in the Treatment of Ice Particle Terminal
518 Velocities, Highlighting Aggregates. *Journal of the Atmospheric Sciences*, **62** (5), 1637–1644,
519 doi:10.1175/JAS3413.1.

520 Mitchell, D. L., P. Rasch, D. Ivanova, G. McFarquhar, and T. Nousiainen, 2008: Impact of
521 small ice crystal assumptions on ice sedimentation rates in cirrus clouds and GCM simulations.
522 *Geophysical Research Letters*, **35** (9), doi:https://doi.org/10.1029/2008GL033552.

523 Mitchell, J. F. B., and W. J. Ingram, 1992: Carbon Dioxide and Climate: Mechanisms of
524 Changes in Cloud. *Journal of Climate*, **5** (1), 5–21, doi:10.1175/1520-0442(1992)005<0005:
525 CDACMO>2.0.CO;2, URL [https://journals.ametsoc.org/view/journals/clim/5/1/1520-0442_](https://journals.ametsoc.org/view/journals/clim/5/1/1520-0442_1992_005_0005_cdacmo_2_0_co_2.xml)
526 [1992_005_0005_cdacmo_2_0_co_2.xml](https://journals.ametsoc.org/view/journals/clim/5/1/1520-0442_1992_005_0005_cdacmo_2_0_co_2.xml), publisher: American Meteorological Society Section:
527 Journal of Climate.

528 Mlawer, E. J., S. J. Taubman, P. D. Brown, M. J. Iacono, and S. A. Clough, 1997: Radiative transfer
529 for inhomogeneous atmospheres: RRTM, a validated correlated-k model for the longwave. *Jour-*
530 *nal of Geophysical Research: Atmospheres*, **102** (D14), 16 663–16 682, doi:10.1029/97JD00237,
531 URL <https://doi.org/10.1029/97JD00237>.

532 Morrison, H., and J. A. Milbrandt, 2015: Parameterization of Cloud Microphysics Based on
533 the Prediction of Bulk Ice Particle Properties. Part I: Scheme Description and Idealized Tests.
534 *Journal of the Atmospheric Sciences*, **72** (1), 287–311, doi:10.1175/JAS-D-14-0065.1.

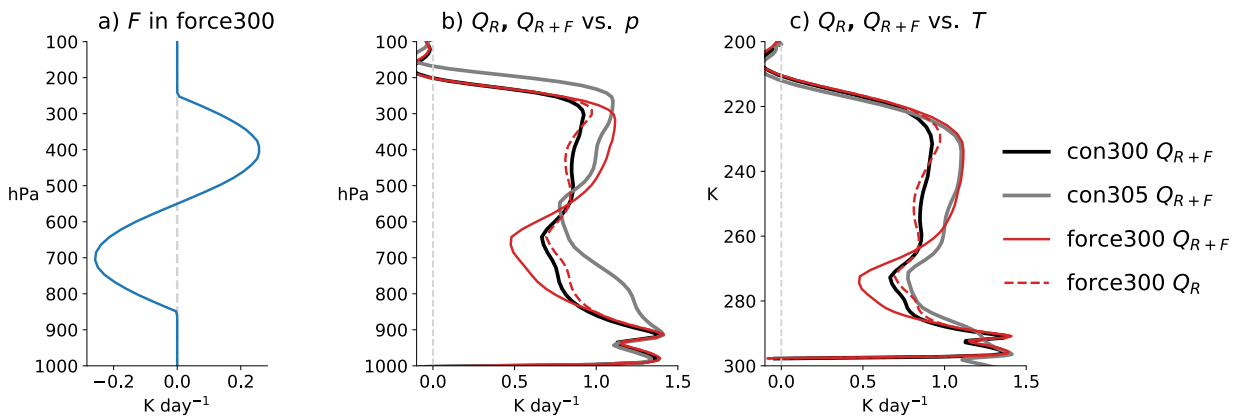
535 Morrison, H., J. A. Milbrandt, G. H. Bryan, K. Ikeda, S. A. Tessendorf, and G. Thompson,
536 2015: Parameterization of Cloud Microphysics Based on the Prediction of Bulk Ice Particle
537 Properties. Part II: Case Study Comparisons with Observations and Other Schemes. *Journal of*
538 *the Atmospheric Sciences*, **72** (1), 312–339, doi:10.1175/JAS-D-14-0066.1.

- 539 Sanderson, B. M., C. Piani, W. J. Ingram, D. A. Stone, and M. R. Allen, 2008: Towards constraining
540 climate sensitivity by linear analysis of feedback patterns in thousands of perturbed-physics GCM
541 simulations. *Climate Dynamics*, **30** (2), 175–190, doi:10.1007/s00382-007-0280-7.
- 542 Schmidt, C. T., and T. J. Garrett, 2013: A Simple Framework for the Dynamic Response of
543 Cirrus Clouds to Local Diabatic Radiative Heating. *Journal of the Atmospheric Sciences*, **70** (5),
544 1409–1422, doi:10.1175/JAS-D-12-056.1.
- 545 Sobel, A. H., J. Nilsson, and L. M. Polvani, 2001: The Weak Temperature Gradient Approximation
546 and Balanced Tropical Moisture Waves. *Journal of the Atmospheric Sciences*, **58** (23), 3650–
547 3665, doi:10.1175/1520-0469(2001)058<3650:TWTGAA>2.0.CO;2.
- 548 Sokol, A. B., and D. L. Hartmann, 2020: Tropical Anvil Clouds: Radiative Driving Toward a
549 Preferred State. *Journal of Geophysical Research: Atmospheres*, **125** (21), e2020JD033 107,
550 doi:https://doi.org/10.1029/2020JD033107.
- 551 Voigt, A., N. Albern, and G. Papavasileiou, 2019: The Atmospheric Pathway of the Cloud-
552 Radiative Impact on the Circulation Response to Global Warming: Important and Uncer-
553 tain. *Journal of Climate*, **32** (10), 3051–3067, doi:10.1175/JCLI-D-18-0810.1, URL https:
554 //journals.ametsoc.org/view/journals/clim/32/10/JCLI-D-18-0810.1.xml, publisher: American
555 Meteorological Society Section: Journal of Climate.
- 556 Wall, C. J., J. R. Norris, B. Gasparini, W. L. Smith, M. M. Thieman, and O. Sourdeval, 2020:
557 Observational Evidence that Radiative Heating Modifies the Life Cycle of Tropical Anvil Clouds.
558 *Journal of Climate*, **33** (20), 8621–8640, doi:10.1175/JCLI-D-20-0204.1.
- 559 Wing, A. A., K. Emanuel, C. E. Holloway, and C. Muller, 2017: *Convective Self-Aggregation in*
560 *Numerical Simulations: A Review*, Vol. 38. Springer Netherlands.

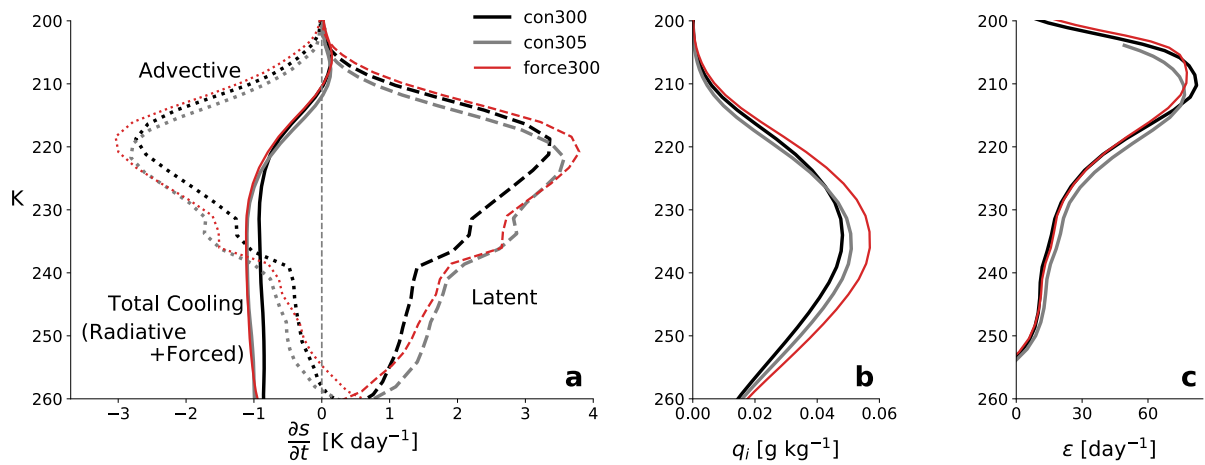
- 561 Wing, A. A., and Coauthors, 2020: Clouds and Convective Self-Aggregation in a Multi-Model
562 Ensemble of Radiative-Convective Equilibrium Simulations. *Journal of Advances in Modeling*
563 *Earth Systems*, doi:10.1029/2020MS002138.
- 564 Zelinka, M. D., and D. L. Hartmann, 2010: Why is longwave cloud feedback positive? *Journal of*
565 *Geophysical Research Atmospheres*, **115** (16), doi:10.1029/2010JD013817.
- 566 Zelinka, M. D., and D. L. Hartmann, 2011: The observed sensitivity of high clouds to mean
567 surface temperature anomalies in the tropics. *Journal of Geophysical Research: Atmospheres*,
568 **116** (D23), doi:https://doi.org/10.1029/2011JD016459.
- 569 Zelinka, M. D., S. A. Klein, and D. L. Hartmann, 2012: Computing and Partitioning Cloud
570 Feedbacks Using Cloud Property Histograms. Part I: Cloud Radiative Kernels. *Journal of*
571 *Climate*, **25** (11), 3715–3735, doi:10.1175/JCLI-D-11-00248.1.
- 572 Zelinka, M. D., D. A. Randall, M. J. Webb, and S. A. Klein, 2017: Clearing clouds of uncertainty.
573 *Nature Climate Change*, **7** (10), 674–678, doi:10.1038/nclimate3402.
- 574 Zhou, W., and S.-P. Xie, 2019: A Conceptual Spectral Plume Model for Understanding Tropical
575 Temperature Profile and Convective Updraft Velocities. *Journal of the Atmospheric Sciences*,
576 **76** (9), 2801–2814, doi:10.1175/JAS-D-18-0330.1.

LIST OF FIGURES

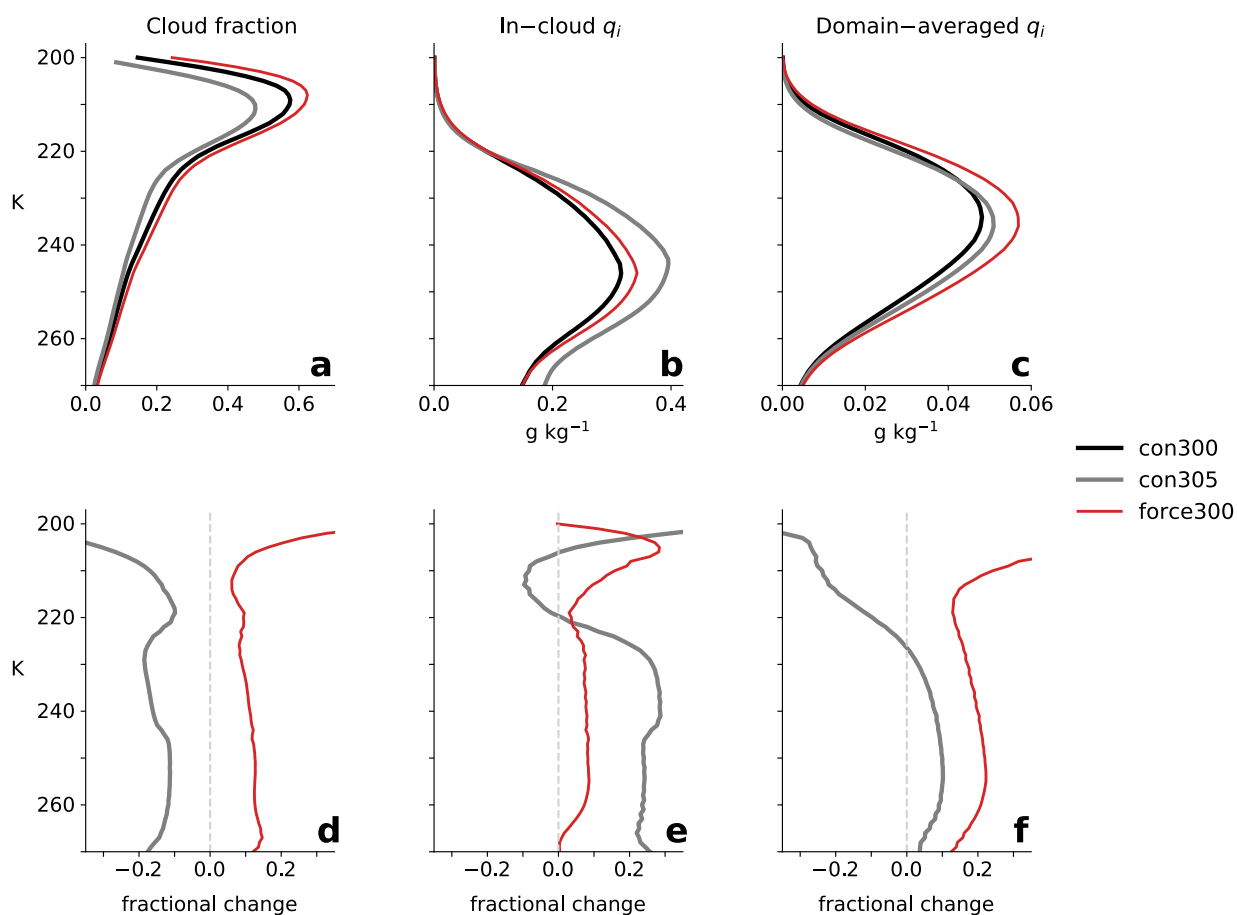
577		
578	Fig. 1.	a) The forced cooling rate F applied in force300. b) Dashed red line: the radiative cooling rate Q_R in force300. Solid lines: the combined radiative and forced cooling rate Q_{R+F} in all three simulations. c) As in b, but as a function of temperature. Note that Q_R and Q_{R+F} are equal in con300 and con305. The radiative cooling rates are for all-sky conditions. 30
579		
580		
581		
582	Fig. 2.	a) Tendencies of the liquid-ice static energy s due to (dashed lines) latent heating, (dotted) advection, and (solid) radiative and forced cooling Q_{R+F} . Tendencies are divided by C_p so that they have units K/day. The sum of the three tendencies is approximately equal to zero in equilibrium, since the diffusive tendency is small. b) Domain-averaged ice mass mixing ratio q_i . c) Latent heating efficiency of ice ϵ given by Eq. (3). 31
583		
584		
585		
586		
587	Fig. 3.	a) Cloud fraction, b) in-cloud ice mixing ratio, and c) domain-averaged ice mixing ratio as a function of temperature in the three simulations. d-f) fractional changes in each quantity with respect to con300. Note: model grid boxes are considered cloudy if the total condensate mixing ratio exceeds 10^{-5} kg kg $^{-1}$ or 1% of the saturation vapor pressure of water, whichever is smaller. 32
588		
589		
590		
591		
592	Fig. 4.	a) Probability density functions (PDFs) of \log_{10} IWP for each simulation. b) Changes in the IWP PDF with respect to con300. 33
593		
594	Fig. 5.	Profiles of each term in Eq. (10) for a) con305 and b) force300. The terms are normalized by C_p so that they are in K/day. Black lines show the total $\Delta\dot{s}_{ice}$ relative to con300, which is equal to the sum of the six individual terms and corresponds to the differences in the latent heating tendencies in Fig. 2a. 34
595		
596		
597		
598	Fig. 6.	Contributions of (blue) non- q_i factors, (green) q_i , and (red) q'_i to changes in the latent heating efficiency ϵ relative to con300 in a) con305 and b) force300. Bold black lines show the total $\Delta\epsilon$, which is equal to the sum of the three colored lines and corresponds to the differences in the ϵ profiles in Fig. 2c. The dashed black line in (a) shows $\Delta\epsilon$ for a modified con305 scenario in which the q_i profile was shifted towards colder temperatures by 1 K. Non- q_i terms include ρ , Γ , V_m , and V'_m 35
599		
600		
601		
602		
603		
604	Fig. 7.	Latent heating efficiency ϵ in the upper troposphere in RCE simulations with different SSTs. 36
605	Fig. 8.	Schematic diagram illustrating this paper's findings. The left side shows a cooler climate, and the right side shows changes that occur with warming. Dashed grey lines are isotherms. The radiative cooling and latent heating rates at a fixed temperature level both increase. As isotherms rise to higher altitudes and lower pressures, the lapse rate Γ and ambient density ρ decrease. Clouds contain a greater amount of ice, but the residence time of ice at any particular temperature shortens. Cloud fraction decreases. 37
606		
607		
608		
609		
610		
611	Fig. B1.	Change in \dot{s}_{ice} relative to con300 calculated using (solid lines) Eq. (9) and (dashed lines) the total differential approximation given by Eq. (10). 38
612		



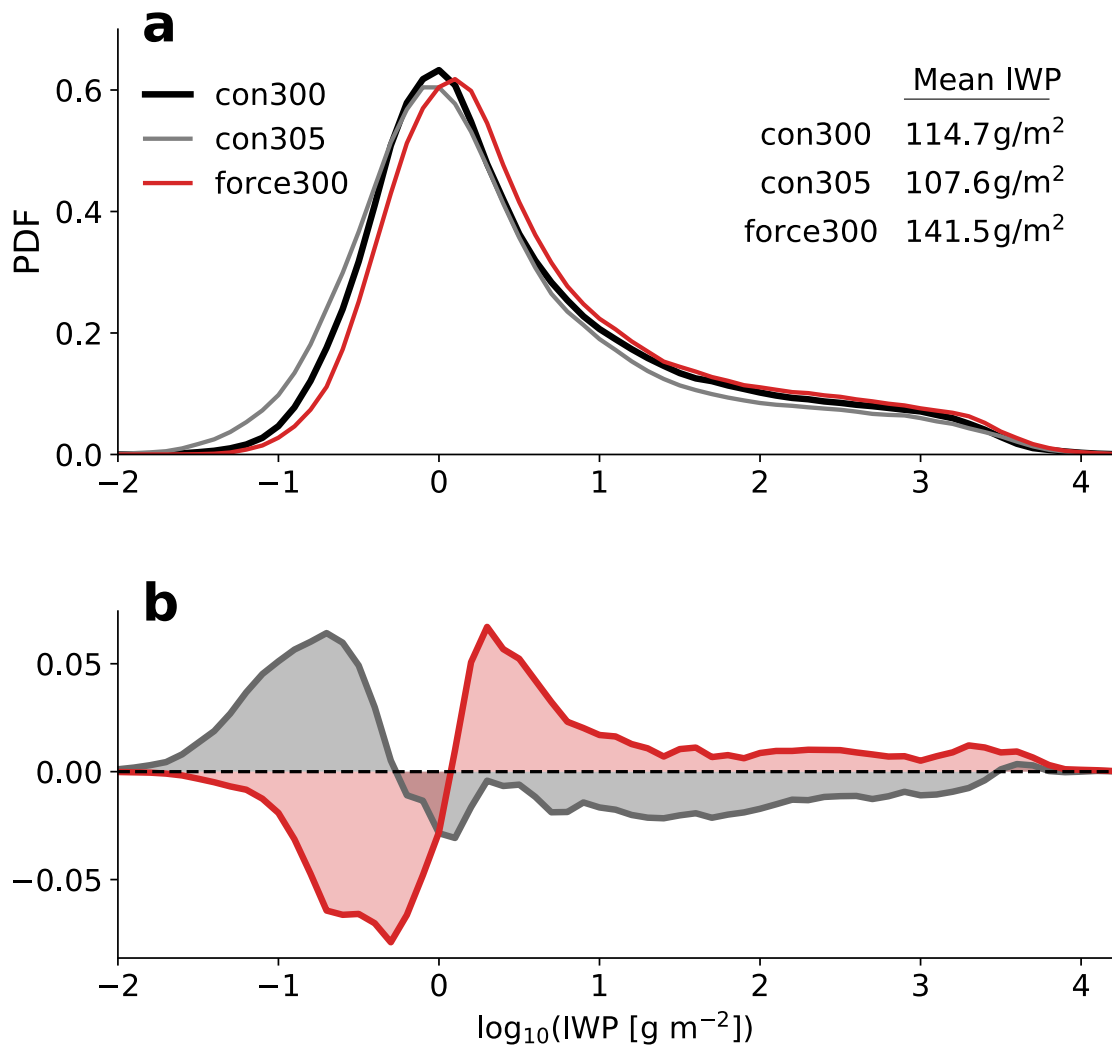
613 FIG. 1. a) The forced cooling rate F applied in force300. b) Dashed red line: the radiative cooling rate Q_R in
 614 force300. Solid lines: the combined radiative and forced cooling rate Q_{R+F} in all three simulations. c) As in b,
 615 but as a function of temperature. Note that Q_R and Q_{R+F} are equal in con300 and con305. The radiative cooling
 616 rates are for all-sky conditions.



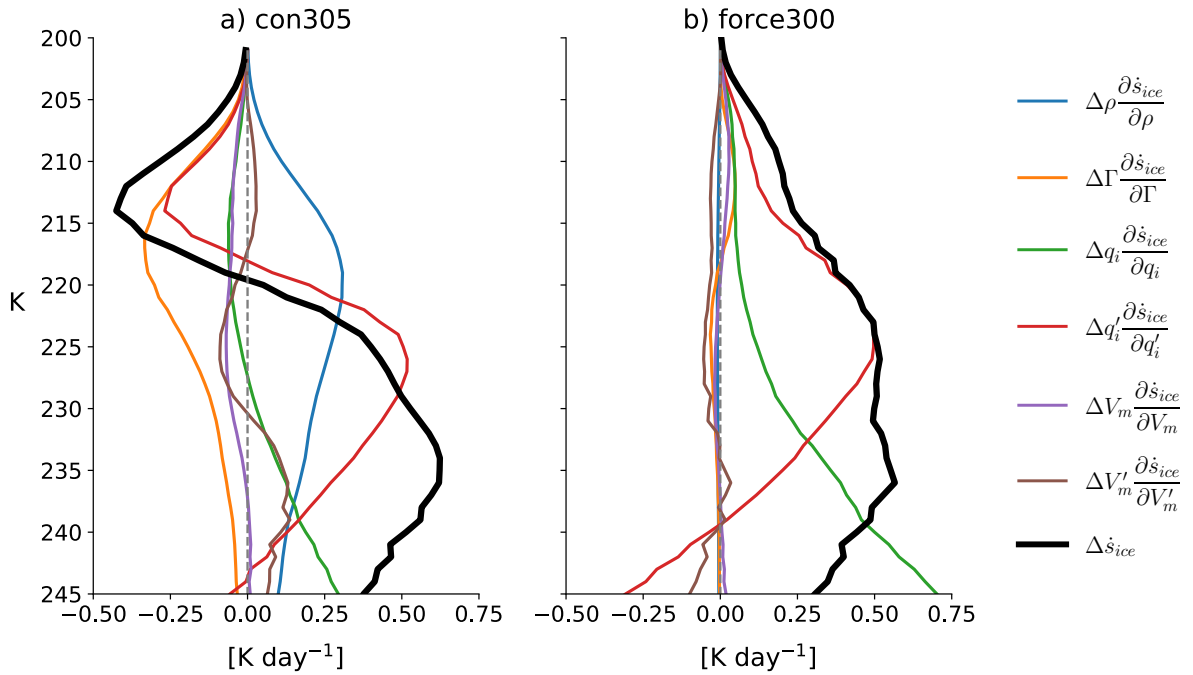
617 FIG. 2. a) Tendencies of the liquid-ice static energy s due to (dashed lines) latent heating, (dotted) advection,
 618 and (solid) radiative and forced cooling Q_{R+F} . Tendencies are divided by C_p so that they have units K/day. The
 619 sum of the three tendencies is approximately equal to zero in equilibrium, since the diffusive tendency is small.
 620 b) Domain-averaged ice mass mixing ratio q_i . c) Latent heating efficiency of ice ϵ given by Eq. (3).



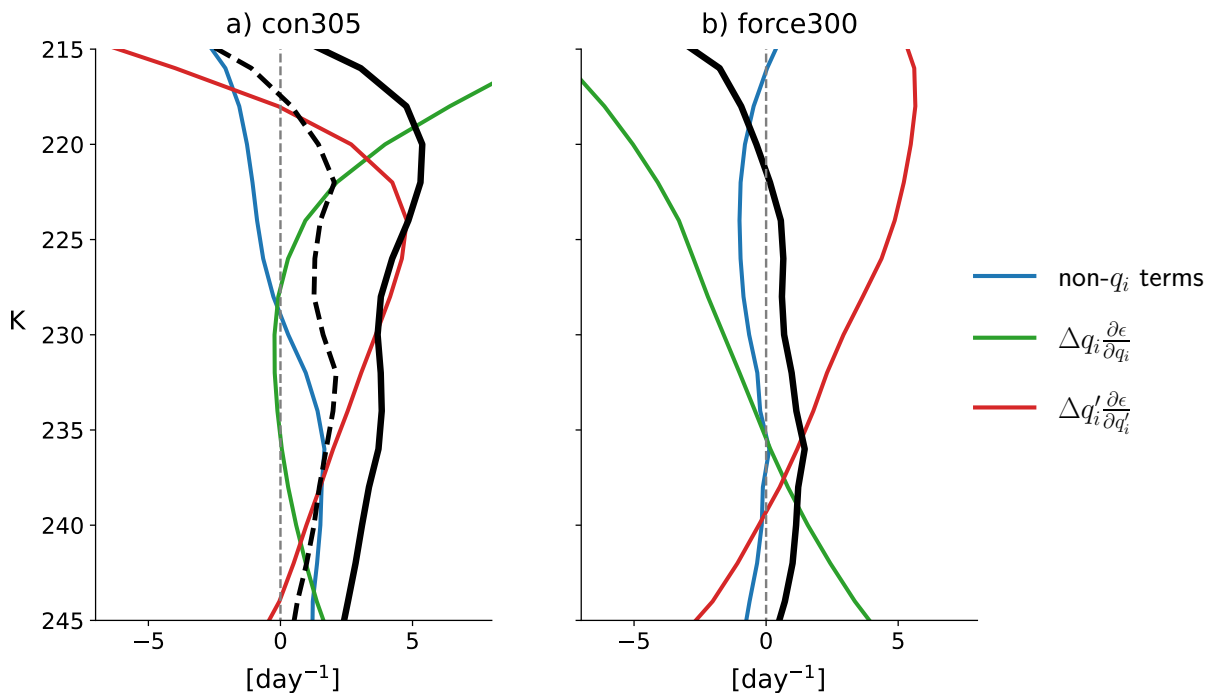
621 FIG. 3. a) Cloud fraction, b) in-cloud ice mixing ratio, and c) domain-averaged ice mixing ratio as a function
 622 of temperature in the three simulations. d-f) fractional changes in each quantity with respect to con300. Note:
 623 model grid boxes are considered cloudy if the total condensate mixing ratio exceeds $10^{-5}\ kg\ kg^{-1}$ or 1% of the
 624 saturation vapor pressure of water, whichever is smaller.



625 FIG. 4. a) Probability density functions (PDFs) of log₁₀IWP for each simulation. b) Changes in the IWP PDF
 626 with respect to con300.



627 FIG. 5. Profiles of each term in Eq. (10) for a) con305 and b) force300. The terms are normalized by C_p so
 628 that they are in K/day. Black lines show the total $\Delta\dot{s}_{ice}$ relative to con300, which is equal to the sum of the six
 629 individual terms and corresponds to the differences in the latent heating tendencies in Fig. 2a.



630 FIG. 6. Contributions of (blue) non- q_i factors, (green) q_i , and (red) q'_i to changes in the latent heating efficiency
 631 ϵ relative to con300 in a) con305 and b) force300. Bold black lines show the total $\Delta \epsilon$, which is equal to the sum
 632 of the three colored lines and corresponds to the differences in the ϵ profiles in Fig. 2c. The dashed black line
 633 in (a) shows $\Delta \epsilon$ for a modified con305 scenario in which the q_i profile was shifted towards colder temperatures
 634 by 1 K. Non- q_i terms include ρ , Γ , V_m , and V'_m .

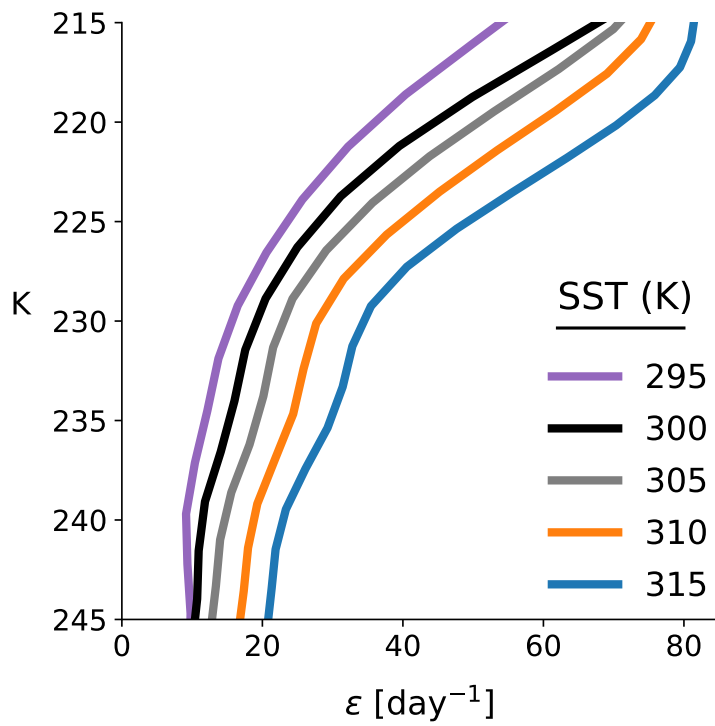
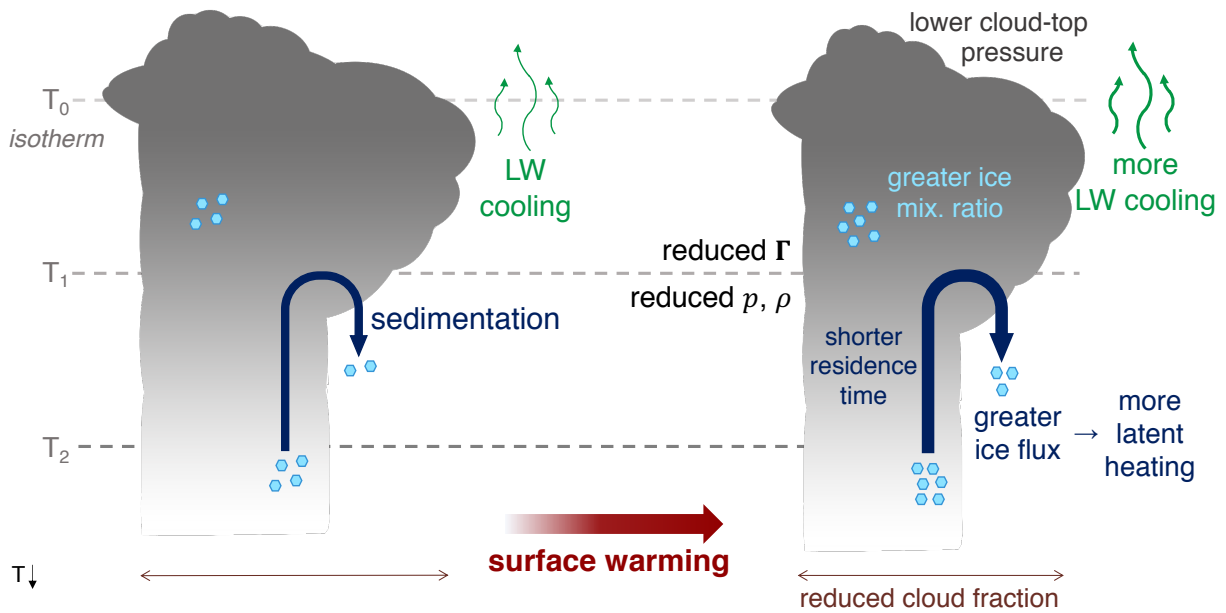
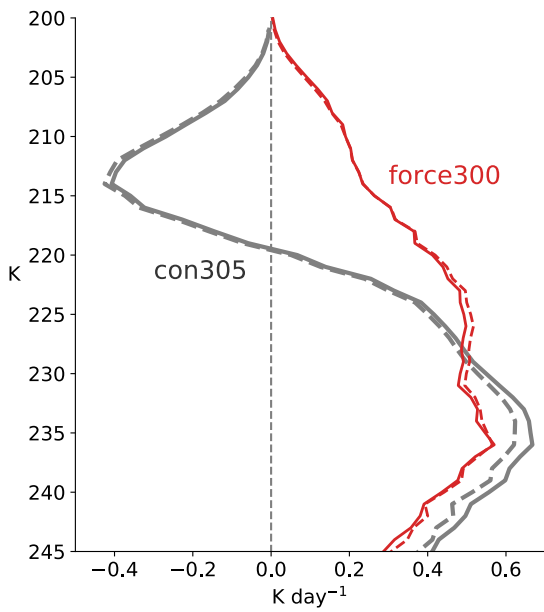


FIG. 7. Latent heating efficiency ϵ in the upper troposphere in RCE simulations with different SSTs.



635 FIG. 8. Schematic diagram illustrating this paper's findings. The left side shows a cooler climate, and the right
 636 side shows changes that occur with warming. Dashed grey lines are isotherms. The radiative cooling and latent
 637 heating rates at a fixed temperature level both increase. As isotherms rise to higher altitudes and lower pressures,
 638 the lapse rate Γ and ambient density ρ decrease. Clouds contain a greater amount of ice, but the residence time
 639 of ice at any particular temperature shortens. Cloud fraction decreases.



640 Fig. B1. Change in s_{ice} relative to con300 calculated using (solid lines) Eq. (9) and (dashed lines) the total
 641 differential approximation given by Eq. (10).